ACS NANO

www.acsnano.org

ARTICLE

Design Principles for Engineering Ionic Liquid-Gold Nanoparticles for Therapeutic Delivery to the Brain

Talia A. Shmool,* Laura K. Martin, Andreas Jirkas, Sophie V. Morse, Claudia Contini, Yuval Elani, and Jason P. Hallett

Cite This: *ACS Nano* 2025, 19, 24806–24816

Read Online

ACCESS | Metrics & More | Article Recommendations | Supporting Information

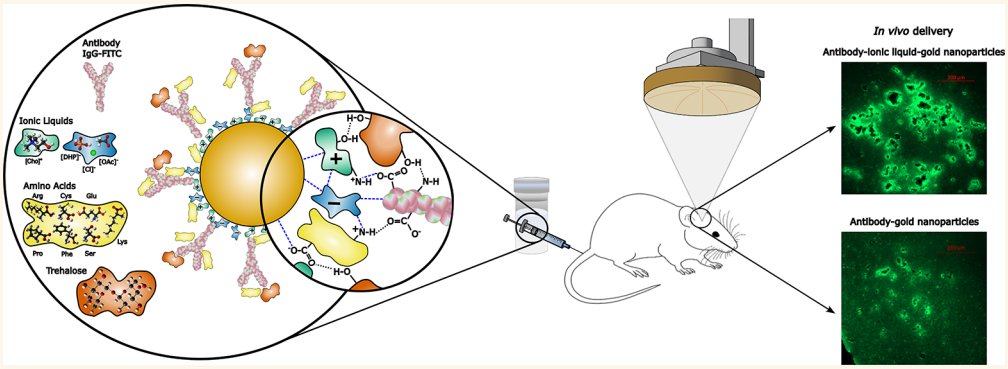

ABSTRACT: **Ionic liquid (IL) nanotechnology holds significant promise for designing nanoscale materials with tunable viscosity, polarity, and thermal stability for advanced therapeutic applications. However, the field currently lacks comprehensive guidelines for integrating ILs into complex therapeutic formulations. Herein, we propose the key design considerations for engineering immunoglobulin G (IgG) conjugated to gold nanoparticles (AuNPs) in the presence of choline-based ILs. By judicious IL cation and anion selection, we fine-tune the supramolecular assemblies and leverage the unique physicochemical properties of ILs to impart AuNPs with advantageous characteristics including enhanced structural, thermal, and thermodynamic stabilities, highly tunable morphologies, and markedly reduced aggregation propensities. Through systematic circular dichroism measurements, the thermodynamic parameters of the complex formulations were determined, offering insight into the IgG conformational changes and design parameters for systems of enhanced IgG conjugation to AuNP surfaces. In demonstrating the power of our design approach, the complex formulation of IgG-choline chloride-AuNPs, also including trehalose, histidine, and arginine, was delivered via focused ultrasound and microbubbles across the blood–brain barrier and showed a 7.6-fold increase in delivery *in vivo* compared to the traditional formulation. We demonstrate that IgG-IL-AuNPs can be easily and precisely manipulated at the nanometer scale, enabling the formation of versatile structural configurations. Holistically, we believe the rational design approach developed will advance the engineering of tailored IL-nanocarriers for targeted therapeutic delivery and broaden the scope of IL applications in biomedicine.**

KEYWORDS: *therapeutic delivery, gold nanoparticles, ionic liquids, amino acids, focused ultrasound, blood–brain barrier*

INTRODUCTION

Ionic liquid (IL) nanotechnology is a nascent field, including the design and engineering of IL-nanoscale materials via a self-assembly approach. ILs are compounds composed of cations and anions, offering unique features including tunable viscosity, polarity, and hydrophobicity and enhanced thermal, structural, and thermodynamic stabilities.[1−3] As such, judicious selection of biocompatible IL cations and anions[4,5] can be exploited in

Received: February 9, 2025
Revised: June 20, 2025
Accepted: June 23, 2025
Published: July 3, 2025

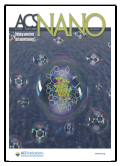

https://doi.org/10.1021/acsnano.5c02375
ACS Nano 2025, 19, 24806–24816

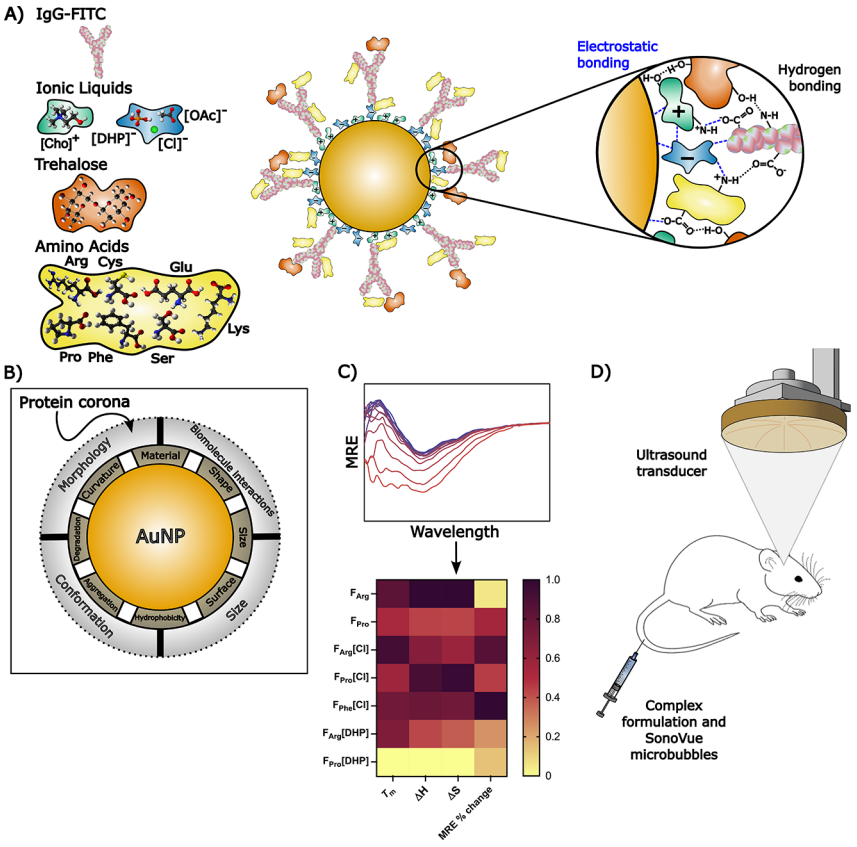

Figure 1. Illustration of the key components of this research. (A) Design and engineering of IgG-IL-AuNPs, with ILs promoting hydrogen bonding and electrostatic conjugation of IgG molecules onto the IL-AuNP surfaces. The disaccharide and amino acid molecules synergistically induce confinement effects for improved IgG-IL-AuNP structural, thermal, and thermodynamic stabilities. (B) Attributes of IL-AuNPs, which can be modified during complex formulation design to yield the formation of protein coronas on the IL-AuNP surfaces, as characterized via TEM experiments. (C) Representative mean residual ellipticity (MRE) spectrum of an IgG-IL-AuNP complex formulation from which the thermodynamic parameters of the system can be calculated and applied in design optimization. (D) *In vivo* delivery of IgG-IL-AuNPs across the blood−brain barrier utilizing focused ultrasound and microbubbles.

molecular design for fine-tuning the self-assembly of novel functional nanomaterials and biomaterials.[6]

While the field of IL nanotechnology is in its infancy, several studies have examined IL structures and functions for therapeutic applications.[7−10] Biocompatible ILs have been explored as building blocks for engineering-tailored nanoarchitectures for therapeutic delivery applications.[11−13] Previous research has demonstrated that diverse imidazolium-based ILs can enhance drug solubility and transdermal delivery and promote the surface functionalization of metal nanoparticles (NPs) for therapeutic applications.[14−17] However, imidazolium-based ILs are of high viscosity, poor biocompatibility, and low biodegradability and can promote protein aggregation,[17] limiting the exploitation of these ILs in pharmaceutical applications. Biocompatible choline-based ILs have been shown to improve therapeutic thermostability, drug solubility, bioavailability, and topical and transdermal drug delivery.[10,18−21] NPs for targeted therapeutic delivery typically require surface functionalization with diverse targeting agents and moieties[22] and chemical modifications of the installed motif and the NPs. This increases the synthetic complexity and limits amendable NP classes and applications. In IL-NP designs, the NPs can consist of lipids, polymers, and inorganic materials, and the ILs can serve as the major frame of the structure to facilitate intermolecular conjugation of peptide and protein molecules to the IL-NP surfaces. This offers opportunities for developing multifunctional NPs for therapeutic delivery via electrostatic conjugation of the therapeutic to the surfaces of NPs, as directed by the IL ions. However, across the IL nanotechnology field, the key design considerations for using ILs as building blocks in complex therapeutic formulations have yet to be comprehensively outlined and require further study.

Herein, we develop a rational thermodynamic-guided approach and outline the key design considerations for utilizing ILs as building blocks for the self-assembly of immunoglobulin G (IgG)-IL-gold nanoparticles (AuNPs) entrapped in a matrix of disaccharide and amino acid molecules. We judiciously selected the biocompatible ILs choline acetate ([Cho][OAc]), choline dihydrogen phosphate ([Cho][DHP]), and choline chloride ([Cho][Cl]) for the construction of a library of IL-AuNPs. On the basis of the physicochemical and structural properties, these biocompatible ILs can facilitate electrostatic conjugation of the IgG molecules to the IL-AuNP surfaces.[23,24] These ILs have also been shown to improve the structural and thermodynamic stabilities of therapeutic formulations, which could aid in enhancing *in vivo* delivery.[10,18,25,26] We utilize AuNPs as the model inorganic NP platform. AuNPs have shown great promise for site-specific therapeutic delivery applications, particularly across the blood−brain barrier (BBB),[27] our selected target site, which poses significant delivery challenges. Notably, focused ultra-

https://doi.org/10.1021/acsnano.5c02375
ACS Nano 2025, 19, 24806−24816

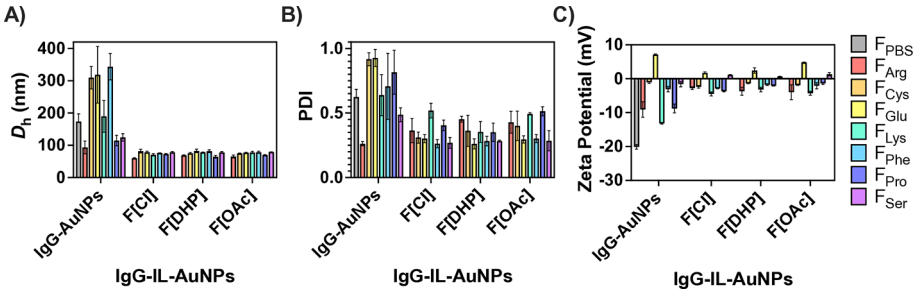

Figure 2. (A) Hydrodynamic diameter (D_h), (B) polydispersity index (PDI), and (C) zeta potential values of complex formulations containing IgG-AuNPs and IgG-IL-AuNPs (Tables S2 and S3). Each complex formulation included trehalose, histidine, and a select amino acid. The ILs included are [Cho][Cl] (F[Cl]), [Cho][DHP] (F[DHP]), and [Cho][OAc] (F[OAc]). Also shown is IgG-AuNPs in phosphate buffered saline (F_{PBS}).

sound (FUS) in combination with microbubbles is a powerful technique for brain-targeted therapeutic delivery.[28−30] Ultimately, we determine the key complex formulation elements for achieving enhanced thermodynamic, thermal, and structural stabilities of IgG-IL-AuNPs and improved FUS-mediated delivery to the brain.[31,32]

In each complex formulation, trehalose, histidine,[33−39] and a select amino acid, specifically arginine (Arg),[40,41] cysteine (Cys),[40,42] glutamic acid,[40,43] lysine (Lys),[40,44−47] phenylalanine (Phe),[40,44,45] proline (Pro),[40,47] and serine (Ser)[40,48] (Tables S1 and S2), are included at proportions previously associated with suppressed therapeutic aggregation for enhanced delivery across the BBB.[34,38−40,42,44,45] The model therapeutic IgG-fluorescein isothiocyanate (FITC) is incorporated with the IL-AuNPs at proportions found to provide surface coverage and increase the structural and thermodynamic stabilities of the system.[18,49−51] Notably, complex formulations composed of these ILs, AuNPs, disaccharides, amino acids, and IgG molecules have yet to be designed.

We conduct dynamic light scattering (DLS), zeta potential, and temperature variable circular dichroism (CD) spectroscopy measurements to determine the aggregation propensity, surface charge, and the structural, thermal, and thermodynamic stabilities of the complex formulations. We perform transmission electron microscopy (TEM) to examine the conjugation of the IgG molecules to the surfaces of the IL-AuNPs. Finally, we deliver the lead complex formulation presenting reduced aggregation propensity and increased structural, thermal, and thermodynamic stabilities across the BBB via FUS and microbubbles. Overall, we set out to present a thermodynamic-guided approach and outline the key design considerations to engineer IL-AuNPs. Additionally, we aim to highlight the role of IL intermolecular interactions in IgG-IL-AuNPs, to ultimately predict the self-assembly processes and advance the engineering of IL-NP structures offering suppressed aggregation, electrostatic conjugation, structural, thermal, and thermodynamic stabilities, and enhanced delivery and accumulation in the brain *in vivo*.

RESULTS AND DISCUSSION

Design and Engineering Complex Formulations. On the basis of thermodynamic principles, IL-AuNP construction would involve the ILs facilitating hydrogen bonding and electrostatic interactions and promoting the conjugation of IgG molecules onto the IL-AuNP surfaces. This would result in the self-assembly of IgG-IL-AuNPs of tunable physicochemical, morphological, and thermodynamic properties (Figure 1A,B).[24] As such, the integrated disaccharide, histidine, and the select amino acid molecules would serve as a matrix surrounding the IgG-AuNPs and IgG-IL-AuNPs and introduce additional multiple intermolecular interactions for suppressed aggregation propensity. Understanding the synergistic hydrogen bonding and electrostatic interactions and the influence of the diverse amino acids on the aggregation propensity and binding of the IgG molecules onto IL-AuNP surfaces[23,52] is key in the development of a robust thermodynamic-guided methodology for designing complex formulations of IgG-IL-AuNPs (Figure 1C). Notably, exploring the impact of the tunable attributes of the IgG-IL-AuNPs on *in vivo* delivery efficacy is critical, as this informs the engineering and optimization of complex formulations in an increasingly specified manner for therapeutic delivery applications (Figure 1D).

Examining Aggregation Suppression and Complex Formulation Surface Charge. The IgG-AuNPs in the complex formulations were examined by DLS measurements and consistently showed relatively higher hydrodynamic diameter (D_h) and polydispersity index (PDI) values compared to complex formulations containing IgG-IL-AuNPs (Figure 2 and Tables S1 and S2). Additionally, contingent on the amino acid, we found that the D_h values for the IgG-AuNPs varied. In the absence of IL, the D_h values increased in the order arginine (F_{Arg}), proline (F_{Pro}), serine (F_{Ser}), phosphate buffered saline (F_{PBS}), lysine (F_{Lys}), cysteine (F_{Cys}), glutamic acid (F_{Glu}), and phenylalanine (F_{Phe}) (Table S3).

Overall, the IgG-[Cho][Cl]-AuNPs showed lower D_h values, increasing for IgG-[Cho][OAc]-AuNPs, and highest for IgG-[Cho][DHP]-AuNPs. Distinctly, this trend was reversed for the IgG-IL-AuNPs in F_{Cys} and F_{Pro}. Notably, IgG-IL-AuNPs in F_{Arg} displayed the lowest D_h values, indicating the greatest aggregation suppression. Additionally, the D_h values were raised for the IgG-IL-AuNPs in the increasing order of F_{Lys}, F_{Pro}, F_{Glu}, F_{Cys}, F_{Ser}, and F_{Phe}. Furthermore, we found consistently lower PDI values for IgG-IL-AuNPs in F_{Phe}, F_{Ser}, and F_{Glu}, increasing for F_{Cys} and F_{Arg}, and highest for F_{Pro} and F_{Lys}. This data evidences the power of ILs as building blocks for constructing complex formulations of IL-AuNPs of suppressed aggregation propensity and controlled D_h and PDI values, which are favorable for intravenous delivery applications.

We found that the IgG-AuNPs in F_{PBS} presented the most negative zeta potential value of the systems examined. Overall, IgG-IL-AuNPs and IgG-[Cho][Cl]-AuNPs exhibited more negative zeta potential values, while IgG-[Cho][OAc]-AuNPs presented more positive zeta potential values. Additionally, the

https://doi.org/10.1021/acsnano.5c02375
ACS Nano 2025, 19, 24806−24816

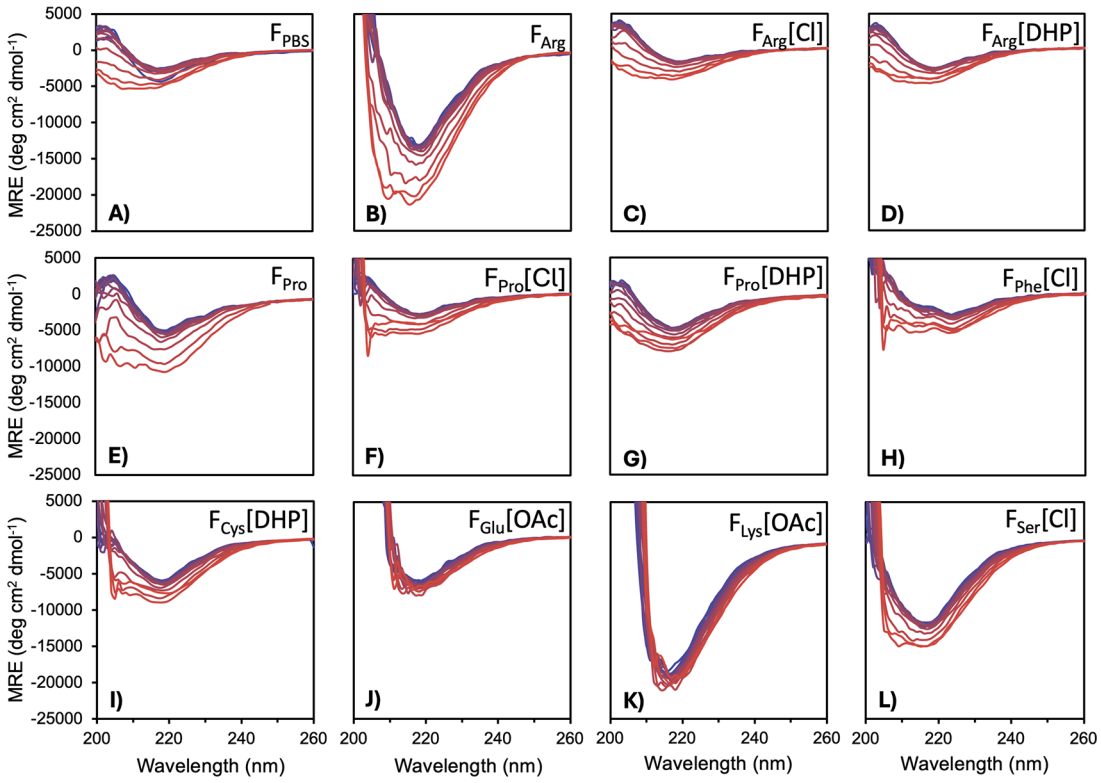

Figure 3. MRE spectra derived from the temperature variable CD data for IgG-AuNPs in F_{PBS} and IgG-AuNPs and IgG-IL-AuNPs in complex formulations. Spectra were measured from 200 to 260 nm with the temperature increasing from 25 °C (blue) to 95 °C (red) in 5 °C increments. See Figure S1 for MRE spectra of additional systems developed. IgG-AuNPs in (A) F_{PBS} and (E) F_{Pro} and IgG-IL-AuNPs in (C) $F_{Arg}[Cl]$, (D) $F_{Arg}[DHP]$, (F) $F_{Pro}[Cl]$, and (G) $F_{Pro}[DHP]$ show a distinct negative absorbance peak at 218 nm indicating β-sheet-rich IgG structures. This feature is reduced in (B) F_{Arg} and (H) $F_{Phe}[Cl]$ and absent in (I) $F_{Cys}[DHP]$, (J) $F_{Glu}[OAc]$, (K) $F_{Lys}[OAc]$, and (L) $F_{Ser}[Cl]$, indicating aggregate assemblies.

zeta potential values were more negative for the IgG-AuNPs and the IgG-IL-AuNPs in $F_{Lys,}$ F_{Pro}, and F_{Arg}, less negative for F_{Cys} and F_{Phe}, and positive zeta potential values were observed for F_{Ser} and F_{Glu}. Notably, for a complex formulation of a given amino acid, the zeta potential value of the IgG-IL-AuNPs was of lower magnitude compared to that of the IgG-AuNPs.

Studying IgG Secondary Structure and Conformational Changes. Systematically examining the mean residual ellipticity (MRE) spectrum of each system (Figure 3 and Figure S1) provided knowledge regarding the key structural features, predictive self-assembly, IgG folding attributes, and conformational changes in the complex formulations. MRE spectra for the IgG-AuNPs in F_{PBS}, F_{Arg}, F_{Pro}, and IgG-IL-AuNPs in $F_{Arg}[DHP]$, $F_{Pro}[DHP]$, $F_{Arg}[Cl]$, and $F_{Pro}[Cl]$ each displayed a β-sheet-rich structure for the IgG molecules, indicated by the distinct negative absorbance peak at 218 nm[53] and positive peak at approximately 200 nm. The near-native IgG structure and suppressed aggregation of the IgG-IL-AuNPs determined via DLS measurements suggest greater structural and colloidal stabilities of the IgG-IL-AuNPs.[54−56] However, in each case, these features gradually degraded upon heating from 25 to 95 °C, attributed to thermal denaturation and the resulting relatively lower structural and colloidal stabilities of these IgG-IL-AuNPs.

The MRE spectra of IgG-AuNPs in F_{Cys} and F_{Phe} and IgG-IL-AuNPs in $F_{Cys}[Cl]$ and $F_{Cys}[DHP]$ suggested that aggregation of the β-sheet structure was present prior to heating (Figure 3 and Figure S1). For the IgG-IL-AuNPs in $F_{Phe}[Cl]$ and $F_{Phe}[DHP]$, we observed a double negative peak at 25 °C between 205 and 225 nm, indicative of α-helices in the secondary structure. In these cases, we also observed a significant loss of spectral features upon heating, evidencing a degree of secondary structural changes due to thermal denaturation. Conversely, IgG-AuNPs in F_{Cys} and F_{Phe} as well as IgG-AuNPs and IgG-IL-AuNPs in F_{Lys}, F_{Glu}, and F_{Ser} exhibited significantly deeper negative peaks at 218 nm and relatively minimal changes with heating (Figure 3 and Figure S1). Based on previous work,[10,18] it is expected that these complex formulations include β-sheet-rich aggregate structures at 25 °C and present thermal denaturation resistance. The IgG-[Cho][OAc]-AuNPs showed limited β-sheet content and negligible structural changes upon heating, also indicating the presence of thermostable aggregate assemblies.

Evaluating the Protein Corona on IL-AuNP Surfaces. We performed TEM experiments to further examine the nanoassemblies of IgG-AuNPs and IgG-IL-AuNPs, which exhibited relatively low D_h and PDI values and varying degrees of the β-sheet structure (Figure 4). For the IgG-IL-AuNPs, we found protein coronas on the surfaces of the [Cho][Cl]-AuNPs in F_{Arg}, F_{Lys}, F_{Pro}, and F_{Ser} and the [Cho][OAc]-AuNPs in F_{Lys}. In contrast, we failed to observe protein coronas on the surfaces of the [Cho][DHP]-AuNPs and the IgG-AuNPs and IgG-IL-AuNPs in F_{Glu} and F_{Phe}. Additionally, the IgG-AuNPs in F_{Arg} presented an irregular-shaped protein corona,[57] and the IgG-AuNPs in F_{PBS} lacked a measurable protein corona on the AuNP surfaces. This was attributed to colloidal aggregation on the TEM grids.[58,59] Additionally, the TEM and CD experiments showed that IgG-IL-AuNPs in $F_{Lys}[OAc]$ and $F_{Lys}[Cl]$

https://doi.org/10.1021/acsnano.5c02375
ACS Nano 2025, 19, 24806−24816

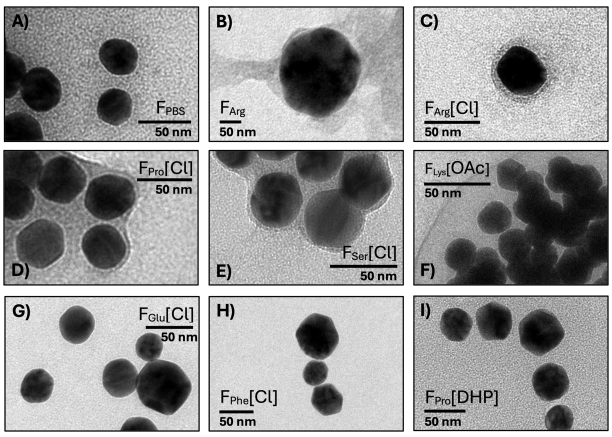

Figure 4. TEM micrographs of IgG-AuNPs in (A) F_{PBS} and (B) F_{Arg}, and complex formulations of IgG-IL-AuNPs. See Figure S2 for micrographs of additional complex formulations. Shown are protein coronas on the surfaces of the [Cho][Cl]-AuNPs in (C) F_{Arg}, (D) F_{Pro}, and (E) F_{Ser} and [Cho][OAc]-AuNPs in (F) F_{Lys}. The protein corona is absent on the surfaces of the [Cho][Cl]-AuNPs in (G) F_{Glu} and (H) F_{Phe} and on the surfaces of (I) [Cho][DHP]-AuNPs in F_{Pro}.

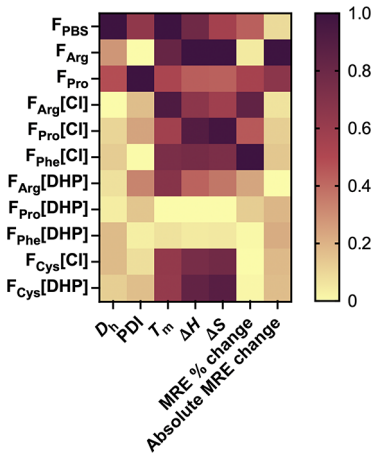

Figure 5. Heatmap showing the hydrodynamic diameter (D_h) and polydispersity index (PDI) values found via DLS measurements, and the melting temperature (T_m), change in enthalpy (ΔH) and entropy (ΔS), relative change in MRE, and absolute change in MRE for the systems exhibiting native and partial secondary structures, as determined via CD spectroscopy measurements. To aid comparison and reveal correlations between parameters, values were scaled from 0 to 1 relative to the range of each variable (absolute values in Table S4).

presented the highest aggregation propensity. Likely, the IgG-IL-AuNPs were entrapped to varying degrees in the trehalose and amino acid matrices, and this influenced the spontaneous self-assembly, intermolecular interactions, and electrostatic conjugation of the IgG-IL-AuNPs, which ought to be accounted for in IL-AuNP design.

Thermodynamic Properties of Complex Formulations. We next determined the relative thermodynamic properties of the IgG-AuNPs and IgG-IL-AuNPs, providing insight into the self-assembly and structural, thermal, and colloidal stabilities of the systems. Specifically, we derived and calculated the melting temperature (T_m) and change in enthalpy (ΔH) and entropy (ΔS) from the temperature variable CD data of the IgG-IL-AuNPs and IgG-AuNPs, as previously described.[10,26] F_{Arg}[Cl], F_{Arg}[DHP], F_{Pro}[Cl], and F_{Pro}[DHP] were chosen for analysis as these exhibited relatively high structural and colloidal stabilities and low D_h and PDI values. For contrast, F_{Cys}[Cl], F_{Cys}[DHP], F_{Phe}[Cl], F_{Phe}[DHP], and the IgG-AuNPs in F_{PBS}, F_{Arg}, and F_{Pro} were also evaluated, as these showed a degree of β-sheet secondary structure, yet displayed distinct structural features and relatively higher D_h values indicative of greater aggregation propensity.

Overall, the T_m values of the complex formulations examined were approximately 80 °C (Table S4), reflecting the thermostable nature of the developed systems. The lowest T_m, ΔH, and ΔS values were found for the IgG-IL-AuNPs in F_{Phe}[DHP] and F_{Pro}[DHP] (5). This can be linked to the lack of protein coronas on the surfaces of the [Cho][DHP]-AuNPs. We consider that the thermodynamic stability is predictive of IgG conjugation to the IL-AuNP surfaces. Notably, the IgG-IL-AuNPs in F_{Arg}[DHP] also possessed relatively low ΔH and ΔS values (Figure 5). Conversely, the IgG-IL-AuNPs in F_{Arg}[Cl] and F_{Pro}[Cl] both showed protein coronas on the surfaces of the [Cho][Cl]-AuNPs and exhibited significantly higher T_m, ΔH, and ΔS values, as well as F_{Phe}[Cl]. These trends were mirrored by the relative change in the MRE spectrum of each system due to heating. Based on the MRE spectra, the IgG-[Cho][Cl]-AuNPs displayed a greater degree of conformational changes compared to equivalent IgG-[Cho][DHP]-AuNP systems. Interestingly, the IgG-IL-AuNPs in F_{Cys}[Cl] and F_{Cys}[DHP] displayed minimal changes in MRE spectral features with heating and demonstrated relatively high T_m, ΔH, and ΔS values. In contrast, the thermodynamic parameters and conformational changes of the IgG-AuNPs in F_{PBS}, F_{Arg}, and F_{Pro} were similar to those of the IgG-[Cho][Cl]-AuNPs. Nonetheless, these systems displayed significantly greater aggregation propensities, as exemplified by the relatively high D_h and PDI values.

***In Vivo* Targeted Delivery of Complex Formulations across the BBB.** On the basis of the reduced D_h and PDI values, visible protein corona, and enhanced structural, thermal, and thermodynamic stabilities, the complex formulation of IgG-[Cho][Cl]-AuNPs in F_{Arg} was selected for FUS-mediated delivery *in vivo* (Figure 6A). Evidence of successful enhanced permeability of the BBB in the left hippocampus (Figure 6B) was observed via the detection of signal from the fluorescently labeled compounds (Figure 6C–E). The opposite right hippocampus, lacking ultrasound, served as a control region, for which fluorescence signal was not detected in the mouse brains. The normalized optical density (NOD) quantification calculated from the obtained images showed that significantly higher *in vivo* delivery was observed for IgG-[Cho][Cl]-AuNPs in F_{Arg} (21.6 ± 11.2) compared to the IgG-AuNPs in F_{Arg} lacking [Cho][Cl] (8.01 ± 4.23) and IgG-FITC in PBS (2.82 ± 1.34). The distribution of the delivered compounds, detected immediately following sonication, was found to be concentrated around the blood vessels in a spot-like pattern, as opposed to uniformly distributed throughout the parenchyma.

Understanding the Design and Thermodynamic Principles to Engineer Complex Formulations of IgG-IL-AuNPs. Judicious IL and amino acid selection implemented during the design process allow for engineering controlled nanoassemblies of IgG-IL-AuNPs. Based on the experimental and thermodynamic data obtained, we propose that the

https://doi.org/10.1021/acsnano.5c02375
ACS Nano 2025, 19, 24806–24816

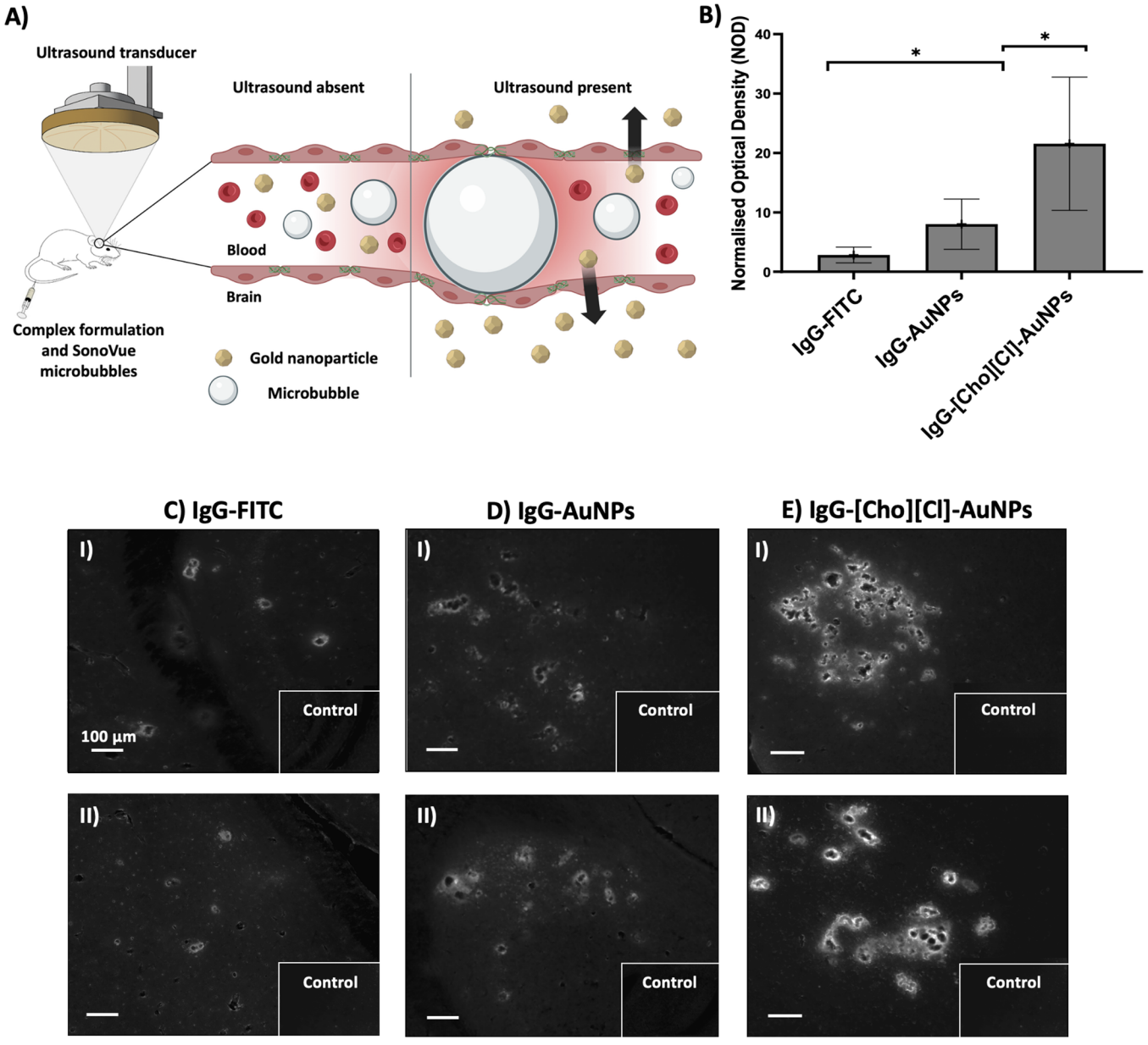

Figure 6. (A) Schematic showing the *in vivo* FUS-mediated delivery of AuNPs into the brain. (B) Fluorescence from the compounds delivered to the brain was quantified by NOD. Fluorescence images (C−E) show the detection of signal from the fluorescently labeled compounds in the left targeted hippocampi and the right hippocampi (control) upon delivering IgG-FITC in PBS, IgG-AuNPs in F_{Arg} lacking IL, and IgG-[Cho][Cl]-AuNPs in F_{Arg}. I and II show two biological replicates for each condition.

presence of ILs promoted the conjugation of IgG molecules onto the AuNP surfaces by mediating an extended network of electrostatic and hydrogen bonding interactions. Conversely, the relatively high D_h and PDI values and lack of protein coronas in the IgG-AuNP systems lacking ILs further highlight the role of the IL ions in facilitating intermolecular interactions contributing to enhanced structural, thermal, and thermodynamic stabilities and IgG conjugation to AuNP surfaces. Notably, this is with the exception of the IgG-AuNPs in F_{Arg}, which exhibited relatively low D_h and PDI values, yet an irregular-shaped protein corona. This is attributed to the positive charge surrounding the planar guanidinium groups of the arginine molecules, contributing to electrostatic interactions, a dominant driving force in peptide association,[60] and amplified upon IL inclusion.

We postulate that [Cho][Cl]-AuNPs mediate the electrostatic interactions in F_{Arg} and F_{Lys}, leading to the conjugation of IgG molecules to the surfaces of [Cho][Cl]-AuNPs. In contrast to the arginine and lysine molecules, the relatively more compact structure of the serine molecules could result in reduced crowding and confinement effects. Consequently, IgG-AuNPs in F_{Ser} possess a greater aggregation propensity and limited thermodynamic and structural stabilities. Nonetheless, the protein corona observed on the surfaces of the [Cho][Cl]-AuNPs in F_{Ser} reflects that [Cho][Cl] effectively mediates electrostatic conjugation of the IgG molecules to the AuNP surfaces. Likely, the proline molecules also facilitate strong hydrophobic interactions with the aggregation prone and surface exposed hydrophobic residues of the IgG molecules. This could result in suppressed aggregation propensity and improved structural and thermodynamic stability of the IgG-

https://doi.org/10.1021/acsnano.5c02375
ACS Nano 2025, 19, 24806−24816

AuNPs in F_{Pro}.[61] Alike, we observed the postulated electrostatic conjugation of the IgG molecules to the surfaces of the [Cho][Cl]-AuNPs in F_{Pro}. Conversely, F_{Glu} showed limited structural and thermodynamic stability, and the relatively more positive surface charge on the AuNPs and IL-AuNPs, in the presence of glutamic acid molecules, would explain the absent protein corona.[62] This could also be attributed to steric repulsions of the glutamic acid chains and disruption of the intermolecular hydrogen bond network in F_{Glu}. Similarly, steric hindrance and hydrophobic effects could result in the lack of electrostatic conjugation of IgG molecules to the surfaces of the IL-AuNPs in F_{Phe}.[63−66]

Compared with the IgG-[Cho][Cl]-AuNPs, we failed to observe conjugation of the IgG molecules onto the surfaces of the [Cho][DHP]-AuNPs, regardless of the amino acid integrated. This could be attributed to the previously identified steric effects and disruption of the intermolecular interactions of [Cho][DHP] inclusive therapeutic formulations.[10,19] Notably, the steric effects of the IL-AuNPs are a key design consideration for electrostatic conjugation of IgG molecules to IL-AuNP surfaces.

Overall, we found limited conjugation of the IgG molecules to the surfaces of [Cho][OAc]-AuNPs; however, F_{Lys}[OAc] and F_{Cys}[OAc] displayed protein coronas on the surfaces of the IL-AuNPs. We consider that the tetrahedral ammonium cations and thiol groups of the lysine and cysteine molecules, respectively, could act as hydrogen bond donors to the acetate anions, thereby facilitating a symmetric charge distribution and strong network of electrostatic and hydrogen bonding interactions.[67−72] This could promote the electrostatic conjugation of the IgG molecules to the surfaces of the IgG-IL-AuNPs in F_{Lys} and F_{Cys}.[73−75] Additionally, the DLS and CD spectroscopy measurements demonstrated significant aggregation for the IgG-IL-AuNPs in F_{Arg}[OAc], which was suppressed for the IgG-IL-AuNPs in F_{Arg}[Cl]. Likely, for the IgG-IL-AuNPs in F_{Arg}[OAc], delocalization of the positive charge surrounding the planar guanidinium groups of the arginine molecules results in disruption of the intricate intermolecular interactions of the IgG-[Cho][OAc]-AuNPs. This could lead to conformational changes and thereby a greater aggregation propensity of the IgG-IL-AuNPs in F_{Arg}[OAc]. Similarly, the IgG-IL-AuNPs in F_{Pro}[OAc] lacked a protein corona despite the IgG-IL-AuNPs in F_{Pro}[Cl] demonstrating conserved secondary IgG structure and protein corona formation. We consider that the solely available proton for hydrogen bonding in the proline molecule is that of the amide group, and the conformational rigidity of the proline side chain could restrict hydrogen bonding with the acetate anions due to the fixed bonding angles and steric bulk. This further emphasized that the electrostatic conjugation of the IgG molecules onto the IL-AuNP surfaces in F_{Pro}[Cl], as opposed to F_{Pro}[OAc], is largely directed via the IL anions, and enhanced structural, thermal and thermodynamic stability, and self-assembly is induced contingent on the identity of the IL ions and amino acid molecules.

We suggest that the restricted aggregation and greater structural, thermal, and thermodynamic stability of the IgG-IL-AuNPs in F_{Arg}[Cl] resulted in the improved FUS-mediated delivery across the BBB compared to the IgG-AuNPs. The *in vivo* delivery achieved for the IgG-IL-AuNPs is in agreement with previous work showing FUS-mediated delivery of agents, above 60 nm, across the BBB.[76−80] However, for the first time, we observed significantly enhanced FUS-mediated delivery of IgG-IL-AuNPs compared to IgG-AuNPs in F_{Arg} and IgG in PBS. We attribute the spot-like pattern observed to the size of the pores within the extracellular matrix of the brain, which are approximately 60 nm in diameter. This would limit the diffusion of large agents within the brain parenchyma once delivered across the BBB. Notably, in future work, employing rapid-short pulses of ultrasound could be used to increase the uniformity of delivery.[81,82]

CONCLUSIONS

In this work, we present a thermodynamic-guided approach and outline the key design considerations for utilizing ILs as building blocks for constructing complex formulations of IgG-IL-AuNPs. By modulating hydrogen bonding and electrostatic interactions of biocompatible ILs and amino acids of diverse physicochemical and structural properties, the IgG molecules were conjugated to the IL-AuNP surfaces, yielding systems offering spontaneous self-assembly, suppressed aggregation, and enhanced structural, thermal, and thermodynamic stability. Improved *in vivo* FUS-mediated delivery and accumulation in the brain were demonstrated for the complex formulation containing IgG-[Cho][Cl]-AuNPs, trehalose, histidine, and arginine molecules. The developed design approach eliminates the requirements of structural modifications of the IgG molecules and enables streamlined functionalization of nanocarrier surfaces, which are challenging to modify via traditional covalent conjugation strategies. We believe that the engineered IgG-IL-AuNPs offer novel opportunities as powerful therapeutic delivery platforms, and our study will advance the nascent field of IL nanotechnology. The insight provided can inform the rational design of IL-nanocarriers to ultimately create ideal platforms for a broad range of delivery applications.

MATERIALS AND METHODS

Materials. [Cho][DHP] was purchased from IoLiTec-Ionic Liquids Technologies GmbH (Heilbronn, Germany). [Cho][Cl], [Cho][OAc], trehalose, L-arginine, L-lysine, L-proline, L-phenylalanine, L-serine, L-cysteine, L-glutamic acid, L-histidine, 40 nm AuNP stabilized suspension in 0.1 mM PBS, and IgG-FITC from human serum (20 mg/mL) were purchased from Sigma-Aldrich Company Limited (Gillingham, Dorset, UK). All chemicals were stored as recommended and used without further purification.

Methods. *Preparation of Complex Formulations.* Stock solutions of [Cho][Cl], [Cho][DHP], and [Cho][OAc] and each formulation buffer were prepared in ultrapure water (ELGA LabWater, High Wycombe, UK) in a glass vial (Thermo Fisher Scientific Inc., Waltham, MA, USA), as reported prior.[10,26] Formulation buffers included 15 mM histidine HCl, 120 mM trehalose, and 75 mM of each of the L-arginine, L-lysine, L-glutamic acid, L-proline, L-serine, L-cysteine, and L-phenylalanine. For electrostatic conjugation, previously reported methodology was adapted and employed.[24,49,83−86] The procedure was performed at 25 °C, utilizing Protein LoBind Eppendorf tubes (Eppendorf, Stevenage, UK), resistant to protein binding.[87] AuNPs, as purchased, were washed and resuspended in the desired IL,[84,86] and the solution was mixed at 500 rpm for 10 min, achieving an IL:AuNP ratio of 1:1%w/v.[49] IgG-FITC was incubated, mixed at 100 rpm with the select formulation buffer for 10 min, added to the IL-AuNPs, and then stirred at 200 rpm for 15 min, followed by washing and resuspension in the select formulation buffer, for an IgG:formulation buffer:IL-AuNPs ratio of 1:17:51%w/v. The centrifugation-based method[88] was avoided to limit shear force, which was found to increase aggregation propensity of the IgG-IL-AuNP systems (Table S5). For each system lacking an IL, the methodology described was also followed with the IL omitted. Finally, the pH of each complex formulation was adjusted to 6.5 by

https://doi.org/10.1021/acsnano.5c02375
ACS Nano 2025, 19, 24806−24816

dropwise addition of hydrochloric acid and sodium hydroxide, confirmed via pH measurements employing the pH electrode Mettler Toledo InLab Micro (WOLFLABS, Pocklington, York, UK). Once prepared, the complex formulations were immediately stored at 4 °C until measured.

Dynamic Light Scattering and Zeta Potential Measurements. For each complex formulation, DLS and zeta potential measurements were performed as previously described.[18] Briefly, DLS measurements were performed to obtain the D_h and PDI values using a Zetasizer Nano ZS (Malvern Panalytical Ltd., Malvern, UK) at a 90° scattering angle, and zeta potential measurements were conducted using a Litesizer 500 (Anton Paar GmbH, Ostfildern, Germany). For each experiment, the average of three measurements is reported.

TEM Experiments. TEM micrographs were obtained employing a JEOL JEM-2100F transmission electron microscope (JEOL, Tokyo, Japan), fitted with a Gatan Prius SC 1000 camera (2 × 4k) (Gatan, Pleasanton, CA, USA). An aliquot of 5 μL of each complex formulation was placed onto a 45 s glow-discharged 200 square mesh carbon-coated copper grid (Agar Scientific, Essex, UK). The grids were blotted with Whatman filter paper after 1 min deposition and imaged using a 2% w/v uranyl acetate solution (Sigma-Aldrich, St. Louis, MO, USA) as a staining agent. The samples were imaged using low electron dose rates to avoid electron beam damage.

CD Spectroscopy Experiments and Calculated Thermodynamic Parameters. Temperature variable CD spectroscopy experiments were performed,[26] and the thermodynamic parameters were derived from the CD measurements as previously outlined.[10] Briefly, samples were heated from 25 to 95 °C, and sequential CD spectra were recorded at 5 °C intervals. The MRE values at 218 nm from smoothed MRE data (OriginLab Corporation, Northampton, MA, USA) were converted into a plot of protein fraction denatured (f_D) at a given temperature using a two-state model of denaturation, assuming equilibrium between the native (N) and denatured (D) protein states, with equilibrium constant (k_D). The CD signal at 218 nm was plotted against the temperature, yielding a sigmoidal plot. For the native state, the region at low-temperature t was approximated to a linear fit

$$y_N = a_N + b_N T$$

where y_N is the predicted CD signal of the native protein at t and a_N and b_N are the temperature independent intercept and gradient, respectively. The equivalent linear relationship between y_D, the predicted CD signal of denatured IgG, and t was derived by calculating a_D and b_D from a linear fit at high t values. y_N and y_D were then calculated for all t. From here, the fraction denatured was calculated as

$$f_D = \frac{(y - y_N)}{(y_D - y_N)}$$

where y was the measured CD signal. This was used to calculate the k_D and Gibbs free energy of denaturation (ΔG_D) as

$$K_D = \frac{f_D}{1 - f_D}$$

$$\Delta G_D = RT \ln K_D$$

for ideal gas constant r. ΔG_D was plotted linearly against temperature in the transition region (-5 kJ mol^{-1} < ΔG_D < 5 kJ mol^{-1}), which describes the behavior of ΔG_D around the denaturation temperature (T_m). The T_m was calculated as the T value for which $\Delta G_D = 0$, as well as estimation of the change in enthalpy (ΔH_m) and entropy (ΔS_m) of denaturation from

$$\Delta G_D = 0 = \Delta H_m - T_m \Delta S_m$$

FUS-Mediated In Vivo Delivery. The experimental protocols outlined herein were approved by the institutional animal facility committee and the UK Home Office regulatory establishments. Twelve female wild-type C57bl/6 mice (10−13 weeks old, 20.3 ± 0.9 g; Envigo, Huntingdon, UK) were used in this study. Mice were treated with FUS and intravenously injected microbubbles (SonoVue, Bracco, Milan, Italy) to deliver the developed complex formulations to the left hippocampus of the brain (n = 3) while using the right hippocampus as the ultrasound lacking control, following a previously described protocol.[82] One MHz ultrasound pulses were emitted at a peak-negative pressure of 0.530 MPa with a pulse length of 10 ms and a pulse repetition frequency of 0.5 Hz, for a duration of 250 s, based on previous work.[81,82] For these ultrasound treatments, a single-element, focused ultrasound transducer (center frequency of 1 MHz, focal depth of 60.5 mm, active diameter of 90 mm, and central rectangular opening of 30 mm × 70 mm H-198, Sonic Concepts, Bothell, WA, USA) was driven by a function generator (33500B, Keysight, Santa Rosa, CA, USA) through a power amplifier (2100L, Electronics and Innovation, Rochester, NY, USA) and a matching network. This setup had previously been calibrated using a needle hydrophone (diameter of 0.2 mm, Precision Acoustics Ltd.) showing an ultrasound beam with a lateral diameter of 2 mm, an elevational diameter of 1 mm, and an axial length of 20 mm defined by the peak-rarefactional pressure full width at half-maximum. Following the ultrasound treatment, mice were transcardially perfused and the brain of each mouse was extracted, sectioned, and imaged with a fluorescence microscope (10×; Zeiss Axio Observer, Oberkochen, Germany).[82] FITC was excited at 470/40 nm, with emissions filtered at 525/50 nm. To quantify differences in the amount of fluorescence detected from the FITC, the NOD was measured for five sections in each brain, as previously described.[82] For the distinct complex formulations, a two-sided Student's t test was performed to determine whether variations in the NODs were significantly different (P < 0.05) between the mice brains. Analysis was conducted using MATLAB R2019b (Mathworks, Natick, MA, USA).

ASSOCIATED CONTENT

Supporting Information

The Supporting Information is available free of charge at https://pubs.acs.org/doi/10.1021/acsnano.5c02375.

Table of abbreviations; chemical structures of the amino acids and the IL ions used; D_h, PDI, and zeta potential values for each system; MRE spectra for each system; T_m, ΔH, and ΔS values derived from the experimental CD spectroscopy data; TEM micrographs for additional select systems; and D_h and PDI values of the complex formulations prepared utilizing an alternative, adapted centrifugation-based method[88] (PDF).

AUTHOR INFORMATION

Corresponding Author

Talia A. Shmool − *Department of Chemical Engineering, Imperial College London, London SW7 2AZ, U.K.*; orcid.org/0000-0002-0415-3050; Email: t.shmool20@imperial.ac.uk

Authors

Laura K. Martin − *Department of Engineering Science, University of Oxford, Oxford OX1 3PJ, U.K.*

Andreas Jirkas − *Department of Chemical Engineering, Imperial College London, London SW7 2AZ, U.K.*

Sophie V. Morse − *Department of Bioengineering, Imperial College London, London SW7 2AZ, U.K.; U.K. Dementia Research Institute at Imperial College London, London W12 0BZ, U.K.*

Claudia Contini − *Department of Life Sciences, Imperial College London, London SW7 2AZ, U.K.*

Yuval Elani − *Department of Chemical Engineering, Imperial College London, London SW7 2AZ, U.K.*; orcid.org/0000-0002-9603-2490

https://doi.org/10.1021/acsnano.5c02375
ACS Nano 2025, 19, 24806−24816

Jason P. Hallett − *Department of Chemical Engineering, Imperial College London, London SW7 2AZ, U.K.;* orcid.org/0000-0003-3431-2371

Complete contact information is available at: https://pubs.acs.org/10.1021/acsnano.5c02375

Author Contributions

T.A.S. and S.V.M. conceived the project. T.A.S. designed the formulations and with A.J. prepared the formulations and performed the DLS, zeta potential, and CD experiments. C.C. performed the TEM experiments, and S.V.M. conducted the *in vivo* study. L.K.M. performed analysis of the CD spectroscopy measurements. T.A.S. and L.K.M. wrote the paper, analyzed the data, and prepared the figures, tables, and Supporting Information. Y.E. and J.P.H. provided comments. All authors approved the manuscript.

Notes

The authors declare no competing financial interest.

ACKNOWLEDGMENTS

T.A.S. and S.V.M. gratefully acknowledge funding from the Dame Julia Higgins Award. Y.E. acknowledges funding from United Kingdom Research and Innovation (UKRI) Future Leaders Fellowship MR/S031537/1 and BBSRC grant BB/W00125X/1. C.C. acknowledges the BBSRC Discovery Fellowship BB/W009323/1.

REFERENCES

(1) Welton, T. Ionic Liquids: A Brief History. *Biophys. Rev.* **2018**, *10* (3), 691−706.
(2) Singh, S. K.; Savoy, A. W. Ionic Liquids Synthesis and Applications: An Overview. *J. Mol. Liq.* **2020**, *297*, No. 112038.
(3) Philippi, F.; Welton, T. Targeted Modifications in Ionic Liquids - From Understanding to Design. *Phys. Chem. Chem. Phys.* **2021**, *23* (12), 6993−7021.
(4) Gomes, J. M.; Silva, S. S.; Reis, R. L. Biocompatible Ionic Liquids: Fundamental Behaviours and Applications. *Chem. Soc. Rev.* **2019**, *48* (15), 4317−4335.
(5) Tzani, A.; Karadendrou, M.-A.; Kalafateli, S.; Kakokefalou, V.; Detsi, A. Current Trends in Green Solvents: Biocompatible Ionic Liquids. *Crystals* **2022**, *12* (12), No. 1776.
(6) Matczuk, M.; Timerbaev, A. R.; Keppler, B. K.; Ruzik, L. Ionic Liquid-Mediated Drug Delivery: A Review on Progress and Challenges Focused on Poly(ionic liquid) Nanoplatforms. *J. Mol. Liq.* **2024**, *399*, No. 124403.
(7) Navti, P. D.; Pandey, A.; Nikam, A. N.; Padya, B. S.; Kalthur, G.; Koteshwara, K. B.; Mutalik, S. Ionic Liquids Assisted Topical Drug Delivery for Permeation Enhancement: Formulation Strategies, Biomedical Applications, and Toxicological Perspective. *AAPS PharmSciTech* **2022**, *23* (5), 161.
(8) Lu, B.; Liu, T.; Wang, H.; Wu, C.; Chen, H.; Liu, Z.; Zhang, J. Ionic Liquid Transdermal Delivery System: Progress, Prospects, and Challenges. *J. Mol. Liq.* **2022**, *351*, No. 118643.
(9) Feder-Kubis, J.; Wirwis, A.; Policht, M.; Singh, J.; Kim, K.-H. Principles and Practice of Greener Ionic Liquid-Nanoparticles Biosystem. *Green Chem.* **2024**, *26* (6), 3072−3124.
(10) Shmool, T. A.; Martin, L. K.; Bui-Le, L.; Moya-Ramirez, I.; Kotidis, P.; Matthews, R. P.; Venter, G. A.; Kontoravdi, C.; Polizzi, K. M.; Hallett, J. P. An Experimental Approach Probing the Conformational Transitions and Energy Landscape of Antibodies: A Glimmer of Hope for Reviving Lost Therapeutic Candidates Using Ionic Liquid. *Chem. Sci.* **2021**, *12* (27), 9528−9545.
(11) Moshikur, R.; Chowdhury, R.; Moniruzzaman, M.; Goto, M. Biocompatible Ionic Liquids and Their Applications in Pharmaceutics. *Green Chem.* **2020**, *22* (23), 8116−8139.
(12) Hu, Y.; Xing, Y.; Yue, H.; Chen, T.; Diao, Y.; Wei, W.; Zhang, S. Ionic Liquids Revolutionizing Biomedicine: Recent Advances and Emerging Opportunities. *Chem. Soc. Rev.* **2023**, *52* (20), 7262−7293.
(13) Moshikur, R.; Carrier, R.L.; Moniruzzaman, M.; Goto, M. Recent Advances in Biocompatible Ionic Liquids in Drug Formulation and Delivery. *Pharmaceutics* **2023**, *15* (4), No. 1179.
(14) Paraskevopoulos, G.; Fandrei, F.; Kumar Pratihast, A.; Paraskevopoulou, A.; Panoutsopoulou, E.; Opálka, L.; Singh Mithu, V.; Huster, D.; Vávrová, K. Effects of Imidazolium Ionic Liquids on Skin Barrier Lipids - Perspectives for Drug Delivery. *J. Colloid Interface Sci.* **2024**, *659*, 449−462.
(15) Chen, X.; Li, Z.; Yang, C.; Yang, D. Ionic Liquids as the Effective Technology for Enhancing Transdermal Drug Delivery: Design Principles, Roles, Mechanisms, and Future Challenges. *Asian J. Pharm. Sci.* **2024**, *19* (2), No. 100900.
(16) Sadaf, A.; Sinha, R.; Ekka, M. K. Ionic Liquid-Mediated Skin Technologies: Recent Advances and Prospects. *Curr. Res. Biotechnol.* **2022**, *4*, 514−529.
(17) Han, Q.; Darmanin, C.; Rosado, C. J.; Veríssimo, N. V.; Pereira, J. F. B.; Bryant, G.; Drummond, C. J.; Greaves, T. L. Structure, Aggregation Dynamics and Crystallization of Superfolder Green Fluorescent Protein: Effect of Long Alkyl Chain Imidazolium Ionic Liquids. *Int. J. Biol. Macromol.* **2023**, *253*, No. 127456.
(18) Shmool, T. A.; Martin, L. K.; Matthews, R. P.; Hallett, J. P. Ionic Liquid-Based Strategy for Predicting Protein Aggregation Propensity and Thermodynamic Stability. *JACS Au* **2022**, *2* (9), 2068−2080.
(19) Shmool, T. A.; Martin, L. K.; Jirkas, A.; Matthews, R. P.; Constantinou, A. P.; Vadukul, D. M.; Georgiou, T. K.; Aprile, F. A.; Hallett, J. P. Unveiling the Rational Development of Stimuli-Responsive Silk Fibroin-Based Ionogel Formulations. *Chem. Mater.* **2023**, *35* (15), 5798−5808.
(20) Riaz, M.; Akhlaq, M.; Naz, S.; Uroos, M. An Overview of Biomedical Applications of Choline Geranate (CAGE): A Major Breakthrough in Drug Delivery. *RSC Adv.* **2022**, *12* (40), 25977−25991.
(21) Caparica, R.; Júlio, A.; Saraiva, N.; Fernandes, A.S.; Machado Araújo, M. E.; Baby, A.R.; Mota, J.; Costa, J. G.; Santos Almeida, T.Choline-Based Ionic Liquids to Deliver Poorly Soluble Drugs in Topical Delivery Systems.*27th EuCheMS Conference on Molten Salts and Ionic Liquids, EuCheMSIL* Lisbon, Portugal, October 7-12, 2018; European Chemical SocietyBrussels, Belgium, **2018**.
(22) Mitchell, M. J.; Billingsley, M. M.; Haley, R. M.; Wechsler, M. E.; Peppas, N. A.; Langer, R. Engineering Precision Nanoparticles for Drug Delivery. *Nat. Rev. Drug Discovery* **2021**, *20* (2), 101−124.
(23) Jazayeri, M. H.; Amani, H.; Pourfatollah, A. A.; Pazoki-Toroudi, H.; Sedighimoghaddam, B. Various Methods of Gold Nanoparticles (GNPs) Conjugation to Antibodies. *Sens. Bio-Sens. Res.* **2016**, *9*, 17−22.
(24) Kumar, S.; Sindhu, A.; Venkatesu, P. Ionic Liquid-Modified Gold Nanoparticles for Enhancing Antimicrobial Activity and Thermal Stability of Enzymes. *ACS Appl. Nano Mater.* **2021**, *4* (3), 3185−3196.
(25) Shmool, T. A.; Constantinou, A. P.; Jirkas, A.; Zhao, C.; Georgiou, T. K.; Hallett, J. P. Next Generation Strategy for Tuning the Thermoresponsive Properties of Micellar and Hydrogel Drug Delivery Vehicles Using Ionic Liquids. *Polym. Chem.* **2022**, *13* (16), 2340−2350.
(26) Shmool, T. A.; Martin, L. K.; Clarke, C. J.; Bui-Le, L.; Polizzi, K. M.; Hallett, J. P. Exploring Conformational Preferences of Proteins: Ionic Liquid Effects on the Energy Landscape of Avidin. *Chem. Sci.* **2021**, *12* (1), 196−209.
(27) Lombardo, S. M.; Schneider, M.; Türeli, A. E.; Günday Türeli, N. Key for Crossing the BBB with Nanoparticles: the Rational Design. *Beilstein J. Nanotechnol.* **2020**, *11*, 866−883.
(28) Burgess, A.; Hynynen, K. Noninvasive and Targeted Drug Delivery to the Brain Using Focused Ultrasound. *ACS Chem. Neurosci.* **2013**, *4* (4), 519−526.

(29) Burgess, A.; Shah, K.; Hough, O.; Hynynen, K. Focused Ultrasound-Mediated Drug Delivery Through the Blood-Brain Barrier. *Expert Rev. Neurother.* **2015**, *15* (5), 477−491.
(30) Chan, T. G.; Morse, S. V.; Copping, M. J.; Choi, J. J.; Vilar, R. Targeted Delivery of DNA-Au Nanoparticles Across the Blood-Brain Barrier Using Focused Ultrasound. *ChemMedChem.* **2018**, *13* (13), 1311−1314.
(31) Ohta, S.; Kikuchi, E.; Ishijima, A.; Azuma, T.; Sakuma, I.; Ito, T. Investigating the Optimum Size of Nanoparticles for Their Delivery into the Brain Assisted by Focused Ultrasound-Induced Blood-Brain Barrier Opening. *Sci. Rep.* **2020**, *10* (1), 18220.
(32) Jo, S.; Sun, I. C.; Ahn, C. H.; Lee, S.; Kim, K. Recent Trend of Ultrasound-Mediated Nanoparticle Delivery for Brain Imaging and Treatment. *ACS Appl. Mater. Interfaces* **2023**, *15* (1), 120−137.
(33) Strickley, R. G.; Lambert, W. J. A Review of Formulations of Commercially Available Antibodies. *J. Pharm. Sci.* **2021**, *110* (7), 2590−2608.e56.
(34) Shmool, T. A.; Batens, M.; Massant, J.; Van den Mooter, G.; Zeitler, J. A. Tracking Solid State Dynamics in Spray-Dried Protein Powders at Infrared and Terahertz Frequencies. *Eur. J. Pharm. Biopharm.* **2019**, *144*, 244−251.
(35) Batens, M.; Shmool, T. A.; Massant, J.; Zeitler, J. A.; Van den Mooter, G. Advancing Predictions of Protein Stability in the Solid State. *Phys. Chem. Chem. Phys.* **2020**, *22* (30), 17247−17254.
(36) Massant, J.; Fleurime, S.; Batens, M.; Vanhaerents, H.; Van den Mooter, G. Formulating Monoclonal Antibodies as Powders for Reconstitution at High Concentration Using Spray-Drying: Trehalose/Amino Acid Combinations as Reconstitution Time Reducing and Stability Improving Formulations. *Eur. J. Pharm. Biopharm.* **2020**, *156*, 131−142.
(37) Shmool, T. A.; Hooper, P. J.; Kaminski Schierle, G. S.; van der Walle, C. F.; Zeitler, J. A. Terahertz Spectroscopy: An Investigation of the Structural Dynamics of Freeze-Dried Poly Lactic-co-glycolic Acid Microspheres. *Pharmaceutics* **2019**, *11* (6), No. 291.
(38) Saurabh, S.; Kalonia, C.; Li, Z.; Hollowell, P.; Waigh, T.; Li, P.; Webster, J.; Seddon, J. M.; Lu, J. R.; Bresme, F. Understanding the Stabilizing Effect of Histidine on mAb Aggregation: A Molecular Dynamics Study. *Mol. Pharmaceutics* **2022**, *19* (9), 3288−3303.
(39) Shmool, T. A.; Woodhams, P. J.; Leutzsch, M.; Stephens, A. D.; Gaimann, M. U.; Mantle, M. D.; Kaminski Schierle, G. S.; van der Walle, C. F.; Zeitler, J. A. Observation of High-Temperature Macromolecular Confinement in Lyophilised Protein Formulations Using Terahertz Spectroscopy. *Int. J. Pharm.: X* **2019**, *1*, No. 100022.
(40) Pereira, R.; Silva, S. G.; Pinheiro, M.; Reis, S.; Vale, M. L. D. Current Status of Amino Acid-Based Permeation Enhancers in Transdermal Drug Delivery. *Membranes (Basel)* **2021**, *11* (5), No. 343.
(41) Rothbard, J. B.; Kreider, E.; VanDeusen, C. L.; Wright, L.; Wylie, B. L.; Wender, P. A. Arginine-Rich Molecular Transporters for Drug Delivery: Role of Backbone Spacing in Cellular Uptake. *J. Med. Chem.* **2002**, *45* (17), 3612−3618.
(42) Meng, Y.; Han, S.; Gu, Z.; Wu, J. Cysteine-Based Biomaterials as Drug Nanocarriers. *Adv. Therap.* **2020**, *3* (5), No. 1900142.
(43) Zhang, Y.; Song, W.; Lu, Y.; Xu, Y.; Wang, C.; Yu, D. G.; Kim, I. Recent Advances in Poly(α-L-glutamic acid)-Based Nanomaterials for Drug Delivery. *Biomolecules* **2022**, *12* (5), No. 636.
(44) Puris, E.; Gynther, M.; Auriola, S.; Huttunen, K. M. L-Type Amino Acid Transporter 1 as a Target for Drug Delivery. *Pharm. Res.* **2020**, *37* (5), 88.
(45) Kou, L.; Bhutia, Y. D.; Yao, Q.; He, Z.; Sun, J.; Ganapathy, V. Transporter-Guided Delivery of Nanoparticles to Improve Drug Permeation across Cellular Barriers and Drug Exposure to Selective Cell Types. *Front. Pharmacol.* **2018**, *9*, No. 27.
(46) Manouchehri, S.; Zarrintaj, P.; Saeb, M. R.; Ramsey, J. D. Advanced Delivery Systems Based on Lysine or Lysine Polymers. *Mol. Pharmaceutics* **2021**, *18* (10), 3652−3670.
(47) Khalid Danish, M.; Gleeson, J. P.; Brayden, D. J.; Byrne, H. J.; Frías, J. M.; Ryan, S. M. Formulation, Characterisation and Evaluation of the Antihypertensive Peptides, Isoleucine-Proline-Proline and Leucine-Lysine-Proline in Chitosan Nanoparticles Coated with Zein for Oral Drug Delivery. *Int. J. Mol. Sci.* **2022**, *23* (19), No. 11160.
(48) Katsumi, H.; Morishita, M.; Yamamoto, A. Development of Serine Modification-Based Kidney-Targeted Drug Delivery System. *Yakugaku Zasshi* **2023**, *143* (2), 121−126.
(49) Boehnke, N.; Dolph, K. J.; Juarez, V. M.; Lanoha, J. M.; Hammond, P. T. Electrostatic Conjugation of Nanoparticle Surfaces with Functional Peptide Motifs. *Bioconjugate Chem.* **2020**, *31* (9), 2211−2219.
(50) Capomaccio, R.; Ojea Jimenez, I.; Colpo, P.; Gilliland, D.; Ceccone, G.; Rossi, F.; Calzolai, L. Determination of the Structure and Morphology of Gold Nanoparticle−HSA Protein Complexes. *Nanoscale* **2015**, *7* (42), 17653−17657.
(51) Mustafaoglu, N.; Kiziltepe, T.; Bilgicer, B. Site-Specific Conjugation of an Antibody on a Gold Nanoparticle Surface for One-Step Diagnosis of Prostate Specific Antigen with Dynamic Light Scattering. *Nanoscale* **2017**, *9* (25), 8684−8694.
(52) Shao, Q.; Hall, C. K. Binding Preferences of Amino Acids for Gold Nanoparticles: A Molecular Simulation Study. *Langmuir* **2016**, *32* (31), 7888−7896.
(53) Greenfield, N. J. Using Circular Dichroism Spectra to Estimate Protein Secondary Structure. *Nat. Protoc.* **2006**, *1* (6), 2876−2890.
(54) Alex, S. A.; Rajiv, S.; Chakravarty, S.; Chandrasekaran, N.; Mukherjee, A. Significance of Surface Functionalization of Gold Nanorods for Reduced Effect on IgG Stability and Minimization of Cytotoxicity. *Mater. Sci. Eng.: C* **2017**, *71*, 744−754.
(55) Liu, W.; Rose, J.; Plantevin, S.; Auffan, M.; Bottero, J.-Y.; Vidaud, C. Protein Corona Formation for Nanomaterials and Proteins of a Similar Size: Hard or Soft Corona? *Nanoscale* **2013**, *5* (4), 1658−1668.
(56) Moore, C. J.; Montón, H.; O'Kennedy, R.; Williams, D. E.; Nogués, C.; Crean, C.; Gubala, V. Controlling Colloidal Stability of Silica Nanoparticles During Bioconjugation Reactions with Proteins and Improving Their Longer-Term Stability, Handling and Storage. *J. Mater. Chem. B* **2015**, *3* (10), 2043−2055.
(57) Nandakumar, A.; Wei, W.; Siddiqui, G.; Tang, H.; Li, Y.; Kakinen, A.; Wan, X.; Koppel, K.; Lin, S.; Davis, T. P.; Leong, D. T.; Creek, D. J.; Ding, F.; Song, Y.; Ke, P. C. Dynamic Protein Corona of Gold Nanoparticles with an Evolving Morphology. *ACS Appl. Mater. Interfaces* **2021**, *13* (48), 58238−58251.
(58) Michen, B.; Geers, C.; Vanhecke, D.; Endes, C.; Rothen-Rutishauser, B.; Balog, S.; Petri-Fink, A. Avoiding Drying-ARtifacts in Transmission Electron Microscopy: Characterizing the Size and Colloidal State of Nanoparticles. *Sci. Rep.* **2015**, *5* (1), No. 9793.
(59) Busch, R. T.; Karim, F.; Weis, J.; Sun, Y.; Zhao, C.; Vasquez, E. S. Optimization and Structural Stability of Gold Nanoparticle-Antibody Bioconjugates. *ACS Omega* **2019**, *4* (12), 15269−15279.
(60) McLain, S. E.; Soper, A. K.; Daidone, I.; Smith, J. C.; Watts, A. Charge-Based Interactions Between Peptides Observed as the Dominant Force for Association in Aqueous Solution. *Angew. Chem., Int. Ed.* **2008**, *47* (47), 9059−9062.
(61) Pal, S.; Mitra, R. K. Investigation on the Rffect of Nonpolar Amino Acids as Macromolecular Crowders on the Stability of Globular Proteins. *Chem. Thermodyn. Therm. Anal.* **2022**, *6*, No. 100044.
(62) Meesaragandla, B.; García, I.; Biedenweg, D.; Toro-Mendoza, J.; Coluzza, I.; Liz-Marzán, L. M.; Delcea, M. H-Bonding-Mediated Binding and Charge Reorganization of Proteins on Gold Nanoparticles. *Phys. Chem. Chem. Phys.* **2020**, *22* (8), 4490−4500.
(63) Moyano, D. F.; Saha, K.; Prakash, G.; Yan, B.; Kong, H.; Yazdani, M.; Rotello, V. M. Fabrication of Corona-Free Nanoparticles with Tunable Hydrophobicity. *ACS Nano* **2014**, *8* (7), 6748−6755.
(64) Ren, J.; Andrikopoulos, N.; Velonia, K.; Tang, H.; Cai, R.; Ding, F.; Ke, P. C.; Chen, C. Chemical and Biophysical Signatures of the Protein Corona in Nanomedicine. *J. Am. Chem. Soc.* **2022**, *144* (21), 9184−9205.
(65) Lin, S.; Li, Y.; Li, B.; Yang, Y. Control of the Handedness of Self-Assemblies of Dipeptides by the Chirality of Phenylalanine and

https://doi.org/10.1021/acsnano.5c02375
ACS Nano 2025, 19, 24806−24816

Steric Hindrance of Phenylglycine. *Langmuir* **2016**, *32* (29), 7420−7426.
(66) Makwana, K. M.; Mahalakshmi, R. Implications of Aromatic-Aromatic Interactions: From Protein Structures to Peptide Models. *Protein Sci.* **2015**, *24* (12), 1920−1933.
(67) Ma, W.; Saccardo, A.; Roccatano, D.; Aboagye-Mensah, D.; Alkaseem, M.; Jewkes, M.; Di Nezza, F.; Baron, M.; Soloviev, M.; Ferrari, E. Modular Assembly of Proteins on Nanoparticles. *Nat. Commun.* **2018**, *9* (1), 1489.
(68) Ditta, S. A.; Yaqub, A.; Tanvir, F.; Rashid, M.; Ullah, R.; Zubair, M.; Ali, S.; Anjum, K. M. Gold Nanoparticles Capped with L-glycine, L-cystine, and L-tyrosine: Toxicity Profiling and Antioxidant Potential. *J. Mater. Sci.* **2023**, *58* (6), 2814−2837.
(69) Xu, J. X.; Alom, M. S.; Yadav, R.; Fitzkee, N. C. Predicting Protein Function and Orientation on a Gold Nanoparticle Surface Using a Residue-Based Affinity Scale. *Nat. Commun.* **2022**, *13* (1), 7313.
(70) Luthuli, S. D.; Chili, M. M.; Revaprasadu, N.; Shonhai, A. Cystein-Capped Gold Nanoparticles Suppress Aggregation of Proteins Exposed to Heat Stress. *IUBMB Life* **2013**, *65* (5), 454−461.
(71) Durocher, S.; Rezaee, A.; Hamm, C.; Rangan, C.; Mittler, S.; Mutus, B. Disulfide-Linked, Gold Nanoparticle Based Reagent for Detecting Small Molecular Weight Thiols. *J. Am. Chem. Soc.* **2009**, *131* (7), 2475−2477.
(72) Řezanka, P.; Řezanková, H.; Matějka, P.; Král, V. The Chemometric Analysis of UV−Visible Spectra as a New Approach to the Study of the NaCl Influence on Aggregation of Cysteine-Capped Gold Nanoparticles. *Colloids Surf. A: Physicochem. Eng. Asp.* **2010**, *364* (1), 94−98.
(73) Biriukov, D.; Futera, Z. Adsorption of Amino Acids at the Gold/Aqueous Interface: Effect of an External Electric Field. *J. Phys. Chem. C* **2021**, *125* (14), 7856−7867.
(74) Futera, Z.; Blumberger, J. Adsorption of Amino Acids on Gold: Assessing the Accuracy of the GolP-CHARMM Force Field and Parametrization of Au−S Bonds. *J. Chem. Theory Comput.* **2019**, *15* (1), 613−624.
(75) Ukmar-Godec, T.; Hutten, S.; Grieshop, M. P.; Rezaei-Ghaleh, N.; Cima-Omori, M. S.; Biernat, J.; Mandelkow, E.; Söding, J.; Dormann, D.; Zweckstetter, M. Lysine/RNA-Interactions Drive and Regulate Biomolecular Condensation. *Nat. Commun.* **2019**, *10* (1), 2909.
(76) Marty, B.; Larrat, B.; Van Landeghem, M.; Robic, C.; Robert, P.; Port, M.; Le Bihan, D.; Pernot, M.; Tanter, M.; Lethimonnier, F.; Mériaux, S. Dynamic Study of Blood-Brain Barrier Closure After its Disruption Using Ultrasound: A Quantitative Analysis. *J. Cereb. Blood Flow Metab.* **2012**, *32* (10), 1948−1958.
(77) Chen, H.; Konofagou, E. E. The Size of Blood-Brain Barrier Opening Induced by Focused Ultrasound is Dictated by the Acoustic Pressure. *J. Cereb. Blood Flow Metab.* **2014**, *34* (7), 1197−1204.
(78) Shen, Y.; Guo, J.; Chen, G.; Chin, C. T.; Chen, X.; Chen, J.; Wang, F.; Chen, S.; Dan, G. Delivery of Liposomes with Different Sizes to Mice Brain after Sonication by Focused Ultrasound in the Presence of Microbubbles. *Ultrasound Med. Biol.* **2016**, *42* (7), 1499−1511.
(79) Guo, J.; Gaoshu, C.; Jinbo, W.; Chien Ting, C.; Shen, Y.; Jian, C.; Yanyan, S. Passive Delivery of Liposomes to Mouse Brain After Blood-Brain Barrier Opening Induced by Focused Ultrasound with Microbubbles. In*2015 IEEE International Ultrasonics Symposium*, IEEE **2015**; pp 1−4.
(80) Aryal, M.; Papademetriou, I.; Zhang, Y. Z.; Power, C.; McDannold, N.; Porter, T. MRI Monitoring and Quantification of Ultrasound-Mediated Delivery of Liposomes Dually Labeled with Gadolinium and Fluorophore Through the Blood-Brain Barrier. *Ultrasound Med. Biol.* **2019**, *45* (7), 1733−1742.
(81) Morse, S. V.; Mishra, A.; Chan, T. G.; de Rosales, R. T. M.; Choi, J. J. Liposome Delivery to the Brain with Rapid Short-Pulses of Focused Ultrasound and Microbubbles. *J. Control. Release* **2022**, *341*, 605−615.
(82) Morse, S. V.; Pouliopoulos, A. N.; Chan, T. G.; Copping, M. J.; Lin, J.; Long, N. J.; Choi, J. J. Rapid Short-Pulse Ultrasound Delivers Drugs Uniformly Across the Murine Blood-Brain Barrier with Negligible Disruption. *Radiology* **2019**, *291* (2), 459−466.
(83) Tam, J. O.; de Puig, H.; Yen, C. W.; Bosch, I.; Gómez-Márquez, J.; Clavet, C.; Hamad-Schifferli, K.; Gehrke, L. A Comparison of Nanoparticle-Antibody Conjugation Strategies in Sandwich Immunoassays. *J. Immunoassay Immunochem.* **2017**, *38* (4), 355−377.
(84) Oliveira, J. P.; Prado, A. R.; Keijok, W. J.; Antunes, P. W. P.; Yapuchura, E. R.; Guimarães, M. C. C. Impact of Conjugation Strategies for Targeting of Antibodies in Gold Nanoparticles for Ultrasensitive Detection of 17β-estradiol. *Sci. Rep.* **2019**, *9* (1), No.13859.
(85) Aubin-Tam, M. E. Conjugation of Nanoparticles to Proteins. *Methods Mol. Biol.* **2013**, *1025*, 19−27.
(86) Ruiz, G.; Tripathi, K.; Okyem, S.; Driskell, J. D. pH Impacts the Orientation of Antibody Adsorbed onto Gold Nanoparticles. *Bioconjugate Chem.* **2019**, *30* (4), 1182−1191.
(87) Davidson, A. M.; Brust, M.; Cooper, D. L.; Volk, M. Sensitive Analysis of Protein Adsorption to Colloidal Gold by Differential Centrifugal Sedimentation. *Anal. Chem.* **2017**, *89* (12), 6807−6814.
(88) Liang, Z.; Zhang, J.; Wang, L.; Song, S.; Fan, C.; Li, G. A Centrifugation-Based Method for Preparation of Gold Nanoparticles and Its Application in Biodetection. *Int. J. Mol. Sci.* **2007**, *8* (6), 526−532.

https://doi.org/10.1021/acsnano.5c02375
ACS Nano 2025, 19, 24806−24816